Astronomy & Astrophysics

Radiative and magnetic properties of solar active regions

I. Global magnetic field and EUV line intensities

A. Fludra[1] and J. Ireland[2]

[1] STFC Rutherford Appleton Laboratory, Space Science and Technology Department, Chilton, Didcot, OX11 0QX, UK
    e-mail: A.Fludra@rl.ac.uk
[2] ADNET Systems, Inc., NASA Goddard Space Flight Center, Mail Code 671.1, Greenbelt, MD 20771, USA
    e-mail: Jack.Ireland@nasa.gov

ABSTRACT

Context. The relationships between the photospheric magnetic flux and either the X-ray or extreme ultraviolet emission from the solar atmosphere have been studied by several authors. Power-law relations have been found between the total magnetic flux and X-ray flux or intensities of the chromospheric, transition region, and coronal emission lines in solar active regions. These relations were then used to infer the mechanism of the coronal heating.

Aims. We derive accurate power laws between EUV line intensities and the total magnetic flux in solar active regions and discuss their applications. We examine whether these global power laws are capable of providing the diagnostics of the coronal heating mechanism.

Methods. This analysis is based on EUV lines recorded by the Coronal Diagnostic Spectrometer (CDS) on SOHO for 48 solar active regions, as they crossed the central meridian in years 1996–1998. Four spectral lines are used: He I 584.3 Å (3×10^4 K), O V 629.7 Å (2.2×10^5 K), Mg IX 368.06 Å (9.5×10^5 K), and Fe XVI 360.76 Å (2.0×10^6 K). In particular, the Fe XVI 360.76 Å line, seen only in areas of enhanced heating in active regions or bright points, has not been used before for this analysis.

Results. Empirical power laws are established between the total active region intensity in the lines listed above and the total magnetic flux. We demonstrate the usefulness of some spatially integrated EUV line intensities, I_T, as a proxy for the total magnetic flux, Φ, in active regions. We point out the approximate, empirical nature of the $I_T - \Phi$ relationships and discuss the interpretation of the global power index. Different power index values for transition region and coronal lines are explained by their different dependence on pressure under the assumption of hydrostatic loop models. However, the global power laws are dominated by the size of the active regions, and we demonstrate for the first time the difficulties in uniquely relating the power index in the global $I_T - \Phi$ relationship to the power index for individual loops and comment on results obtained by other authors. We caution against using global power laws to infer the coronal heating mechanism without a detailed knowledge of the distributions of the magnetic flux densities and instrumental response as a function of temperature. Despite these uncertainties, we show that the intensities of the transition region lines in individual loops depend on the photospheric magnetic flux density, ϕ, through $I_{tr} \propto \phi^{\delta_t}$, $\delta_t < 1$, and the coronal line Fe XVI, $I_{Fe} \propto \phi^{\delta_c}$, $\delta_c > 1$, and under the assumption of hydrostatic loops we can place a constraint on the coronal heating models, obtaining the volumetric heating rate, E_H (erg cm^{-3} s^{-1}), $E_H \propto \phi^\gamma$, where $0.6 < \gamma < 1.1$.

Key words. Sun: UV radiation – Sun: magnetic fields – Sun: corona – Sun: transition region

1. Introduction

In the search for the coronal heating mechanism over the past three decades, relationships between the X-ray and EUV line emission and the photospheric magnetic field in solar active regions have been studied by many authors. The expectation was that if well-defined relationships existed, they could be compared to theoretical predictions from the many models of coronal heating and provide constraints to identify the correct model.

Past research has shown that the total intensity of EUV spectral lines or a broad-band X-ray flux summed over an entire active region are related to the global magnetic quantities. Gurman et al. (1974) studied OSO-6 data and found that the Mg X line intensity is proportional to the magnetic flux density. Golub et al. (1980) found a relationship between the coronal thermal energy content and the total magnetic flux, and between pressure and magnetic flux density, using soft X-ray observations from Skylab. Schrijver (1987) used Skylab data which included a chromospheric C II line, a coronal Mg X line and soft X-ray

emission and found power laws relating integrated intensities to the total magnetic flux Φ, with the power index dependent on formation temperature of the spectral line (chromosphere, transition region or corona). Fisher et al. (1998) explored correlations between the total X-ray luminosity observed by the Yohkoh Soft X-ray Telescope and three quantities: the total magnetic area, the total unsigned magnetic flux, and the total B^2 for 330 active regions. Pres & Phillips (1999) showed how a temporal evolution of the total Fe XII 195 Å flux in SOHO-EIT of a coronal bright point matches that of the total magnetic flux. Yashiro & Shibata (2001) analysed soft X-ray emission from the Yohkoh SXT telescope, refining the analysis of Golub et al. (1980) to derive the dependence of the thermal energy and pressure on Φ and B, respectively. Fludra et al. (2002) presented for the first time relationships between the EUV spectral lines from the SOHO Coronal Diagnostic Spectrometer and the magnetic flux in active regions. Subsequently, Fludra & Ireland (2003) derived a refined relationship for an Fe XVI line and proposed a

new method of deducing an $I-B$ dependence for individual loops from the spatially integrated intensities. Benevolenskaya et al. ([2002](#)) studied the dependence of soft X-ray and EUV emission from SOHO-EIT on the magnetic flux over the solar cycle. Schrijver & Aschwanden ([2002](#)a) performed a large simulation of the coronal magnetic fields and modelled the expected X-ray emission for different coronal heating models, comparing it to the many X-ray solar and stellar observations, in an attempt to directly test the heating mechanism. van Driel-Gesztelyi et al. (2003) describe a long-term evolution of one active region and study the dependence of plasma parameters derived from X-ray data on the mean magnetic flux density. Saar ([2001](#)) found a similar dependence between ROSAT X-ray fluxes and the magnetic field in a sample of K and M stars, and Pevtsov et al. ([2003](#)) presented a combined dependence of X-ray radiance on the magnetic flux for the quiet sun, solar active regions and a range of stellar objects.

As a result of past research, the existence of power laws of the following form: $I_T \propto \Phi^\alpha$, where I_T are either broad band fluxes or spectral line intensities, has been established with varying degree of accuracy. Such correlations between the EUV or X-ray emission and the magnetic flux are regarded by most authors as a proof that the magnetic field plays an active role in the coronal heating and, subsequently, attempts are made to derive the heating mechanism. Early studies of relationships between the soft X-ray emission and the magnetic flux used the total radiative losses in soft X-rays as an approximation of the total radiative output from an active region, and compared it to the total power dissipated in the region, estimated from the Poynting flux predicted by theoretical models of coronal heating. Other studies estimate electron temperatures and emission measures, averaged over active regions area, and compare them to loop scaling laws. In essence, all these papers attempt to solve an inverse problem of determining the dependence of the heating rate on the magnetic field, B, from the observed dependence of spatially integrated radiative quantities (line intensities or broad band fluxes) on the spatially integrated magnetic flux, Φ.

Huge simplifications are made in these analyses. First, it is typically overlooked that magnetic loops serve as a container for the plasma and, as shown below, the overwhelming part of the $I_T - \Phi$ correlation arises due to a geometrical dependence. Second, a variety of ad hoc approaches to calculating the spatially-integrated or spatially-averaged radiative and magnetic quantities and the interpretation of the global $I_T - \Phi$ relationships can be found in the literature. The current confusion in this subject and the difficulty with deducing the coronal heating mechanism is well illustrated by the conflicting results – while many papers favour the proportionality of the volumetric heating rate E_H to B, Demoulin et al. ([2003](#)) conclude from a comprehensive study that E_H is proportional to B^2.

A second, more elaborate approach to the coronal heating problem involves forward modelling that includes magnetic field extrapolations, then hydrostatic modelling of coronal loops by assuming a parametric dependence of the heating rate on B and the loop length, L, and calculating the total radiative losses (Schrijver et al. [2004](#)) or the response of X-ray and EUV instruments (Warren & Winebarger [2006](#)). The modelled quantities are subsequently compared to the observed intensities for different values of parameters defining the heating rate.

In this paper we address the first category of studies, i.e., the mathematical inversion of global power laws, $I_T - \Phi$. While we do not attempt to arbitrate between different past approaches to the study of the coronal heating, we first present a simpler but

necessary step of assessing the suitability of the global power laws for the task of testing the coronal heating mechanism.

The main aim of the present paper is to present the relationship between the total magnetic flux and EUV line intensities observed by the Coronal Diagnostic Spectrometer (CDS) on SOHO and to analyse the usefulness and diagnostic capability of these global relationships of the form $I \propto \Phi^\alpha$. We also discuss previous results available in the literature and show that some of them offer only a rough qualitative dependence between the magnetic field and intensities, and cannot be used for quantitative studies of the coronal heating.

We address the following questions: (1) which EUV lines are the best proxies for the total magnetic flux in an active region; (2) what are the physical reasons to expect a power law dependence between the total line intensity and the total magnetic flux; (3) how does the power index in the global $I_T - \Phi$ relationship relate to the power index in the $I - \phi$ relationship for individual coronal loops; (4) is the global power index capable of diagnosing the coronal heating mechanism?; (5) how to interpret the different values of the power index in the global $I_T - \Phi$ relationship for different EUV spectral lines; (6) discussion of analysis errors and assumptions that may lead to incorrect values of the power index.

The calibrated data from the Coronal Diagnostic Spectrometer on SOHO offer an unique opportunity to study spectral lines not previously used in this type of analysis. Since the beginning of the SOHO mission, CDS has carried out a synoptic observation of the central solar meridian, with a $4'$-wide field of view. The CDS synoptic observation includes He I 584.3 Å (30 000 K), O V 629.7 Å (transition region, 2×10^5 K), Mg IX 368.06 Å (corona, 9.5×10^5 K), and Fe XVI 360.76 Å (hot corona, 2×10^6 K). We examine 48 active regions in EUV emission, significantly exceeding the number studied in the only previous study of EUV/total unsigned magnetic flux correlations and power laws. The analysis uses different spectral lines than those observed by Skylab and used by Schrijver et al. ([1985](#)) and Schrijver ([1987](#)). Note that while three of the four lines used here cover similar temperatures to those in the previous EUV study, the Fe XVI 360.76 Å line is unique – its peak emissivity is at 2 million degrees and it offers a good diagnostic of active region temperatures. This is in contrast to the one-million degree line available in this study, which is shown to be a less useful diagnostic. The combination of a hot coronal line (Fe XVI) and a transition region line (O V) is not available in any other instrument and provides a unique diagnostic capability.

The following section demonstrates how emission in each of these lines is related to the heating rate.

2. Intensity dependence on pressure and heating rate

The energy emitted in a coronal EUV line, for example, Fe XVI 360.76 Å, is over ten times smaller than the total energy of soft-X-rays in the range 1–300 Å (observed by Yohkoh SXT) and cannot be directly used as a measure of the total radiative losses. However, one can use loop models to deduce the line intensity dependence on the heating rate, and then derive the dependence of the heating rate on the magnetic flux density. A rather narrow temperature dependence of EUV line emissivities, $G(T)$, compared to that of a broad band X-ray instrument, means that the EUV emission can be localised at a given temperature and height of a coronal loop (e.g., loop legs or loop apex).

We assume that the active region loops with apex temperatures higher than 1.6×10^6 K are in a static equilibrium. This was found true for X-ray loops (Porter & Klimchuk 1995) and further shown to be compatible with coronal observations by Schrijver et al. (2004). The consequences of this assumption for our data are explored in this section. Possible deviations from the assumption of static loops with constant cross-section are discussed in Sect. 7.3.

The line intensity $I(z)$ at a distance $(z, z + \mathrm{d}z)$ along a loop, measured from the loop footpoint, is:

$$I(z)\mathrm{d}z = A_{\mathrm{el}} S_{\mathrm{cs}} N_{\mathrm{e}}^2(z) G(T(z))\mathrm{d}z \tag{1}$$

where A_{el} is the element abundance relative to hydrogen, $G(T)$ is the line emissivity and S_{cs} is a constant loop cross-section. The electron density is expressed as $N_{\mathrm{e}}(z) = P/(2k_{\mathrm{B}}T_{\mathrm{e}}(z))$, where pressure P is assumed to be constant along the loop, and k_{B} is the Boltzmann's constant. Thus, the total line intensity I_{L} emitted from the whole loop is

$$I_{\mathrm{L}} = \frac{2A_{\mathrm{el}}S_{\mathrm{cs}}}{4k_{\mathrm{B}}^2} \times P^2 \int_0^L \frac{G(T(z))}{T^2(z)} \mathrm{d}z \tag{2}$$

where the integration takes place from the loop footpoint ($z = 0$) to the loop top ($z = L$), and intensities from both halves of the loop have been added. The $G(T)$ functions are available from standard atomic physics packages: ADAS (Summers 1993) or Chianti (Dere et al. 1997).

Substituting the temperature T for the distance z, we can write:

$$I_{\mathrm{L}} = \frac{A_{\mathrm{el}}S_{\mathrm{cs}}}{2k_{\mathrm{B}}^2} P^2 \int_{T1}^{T2} \frac{G(T)}{T^2} \left(\frac{\mathrm{d}z}{\mathrm{d}T}\right) \mathrm{d}T \tag{3}$$

where T_1, T_2 are temperatures corresponding to the integration limits on z.

Following Martens et al. (2000, their Eq. (21)) we assume that the temperature in the transition region of a static loop varies as:

$$T(z) = 1.29 \times T_{\mathrm{max}}(z/L)^{1/3}. \tag{4}$$

An almost identical approximation can be obtained from Aschwanden & Schrijver (2002b, their Eq. (19)), assuming their $a = 2.0$, $b = 0.33$ and neglecting the quadratic term $(z/L)^2$ in the expansion of $(1 - z/L)^2$.

Equation (3) can be further modified, assuming that the loops are in static equilibrium and using the loop scaling laws. The basic form of scaling laws is (Rosner et al. 1978; Martens et al. 2000):

$$PL = (T_{\mathrm{top}}/C_0)^3 \tag{5}$$

$$E_{\mathrm{H}} = C_1 P^{7/6} L^{-5/6} \tag{6}$$

where T_{top}, N_{top} are the electron temperature and density at the loop apex, E_{H} is the volumetric heating rate averaged over the whole loop, L is the loop half-length, $C_0 = 1450$, $C_1 = 1.1 \times 10^5$ in cgs units (Martens et al. 2000). The pressure $P = 2k_{\mathrm{B}}N_{\mathrm{e}}T_{\mathrm{e}}$ is assumed constant along the loop. For completeness, we point out that Eqs. (1)–(3) and (7) define the intensity of a single spectral line which is proportional to the abundance of the element. Equations (5) and (6) do not contain explicit references to abundances because they are scaling laws that have been derived from the energy equation, and the constants of proportionality C_0 and C_1 depend on the radiative loss function which is dominated by

several elements (Fe, C, N, O). Therefore, C_0 and C_1 depend indirectly on the chosen set of abundance values (see, e.g., Martens et al. 2000).

Computing $\mathrm{d}T/\mathrm{d}z$ from Eq. (4) and using the scaling law (Eq. (5)) one obtains intensity of a transition region line

$$I_{\mathrm{tr}} = \frac{3A_{\mathrm{el}}S_{\mathrm{cs}}}{2k_{\mathrm{B}}^2 1.29^3 C_0^3} P \int_{T1}^{T2} G(T)\mathrm{d}T. \tag{7}$$

This demonstrates, as pointed out by Hammer (1992) and elaborated by Martens et al. (2000), that intensities of lines emitted in the transition region are proportional to pressure. Since, for a static loop, pressure is related to the average heating rate (Eq. (6)), the line intensity can be expressed as a function of E_{H} and L, and this can be compared to the observed dependence on ϕ and L.

Below we show that the intensity of the coronal line Fe XVI is proportional to P^2 when the loop-top temperature is in the range 2.0–2.5×10^6 K. We simulate a distribution of intensity of the Fe XVI 360.76 Å line along a static loop for loop-top temperatures between 1.6×10^6 K and 3.0×10^6 K, using a static loop model described by Martens et al. (2000) and a temperature distribution along the loop provided by Martens (2001, private communication). For temperatures up to 2.0×10^6 K the peak of the Fe XVI intensity is reached at the loop top. For higher temperatures, the peak intensity gradually moves away from the loop top towards the footpoints. For example, for $T_{\mathrm{top}} = 2.5 \times 10^6$ K, the intensity peaks at 0.3 of the distance between the footpoint and the loop top, and the intensity at the top is approximately only half of the maximum intensity. This simulated behaviour of the Fe XVI intensity distribution along the loop suggests that the loops observed by CDS in the Fe XVI line cannot be significantly hotter than 2×10^6 K. If they were, the spatial distribution of intensities would show double-peaked features, with intensity peaks concentrated towards the magnetic footpoints, with lower intensities at loop tops, i.e., the pattern that is characteristic of the observed Mg IX emission (Fig. 1c) but that is not seen in Fe XVI.

We find that the dependence of the Fe XVI intensity on pressure varies depending on the peak temperature in the loop and can be approximated as $I_{\mathrm{L}} \propto P^\epsilon$. Approximate values of the power index ϵ are given in Table 1 for several temperature intervals, showing that the Fe XVI intensity increases steeply with pressure for temperatures below 1.9×10^6 K, is proportional to P^2 for temperatures 2.0–2.5×10^6 K, and becomes proportional to pressure for loop apex temperatures greater than 3×10^6 K. The dependence of line intensities on pressure was discussed by Martens et al. (2000) who show that for loop-top temperatures greater than 2×10^6 K, the total intensity of lines emitted in loop legs at temperatures of 10^6 K or lower (e.g., Mg IX) is proportional to pressure. Extending this argument, if $T_{\mathrm{top}} > 3 \times 10^6$ K then the intensity of the hotter line of Fe XVI also becomes proportional to pressure. However, at temperatures greater than 3×10^6 K the Fe XVI emission would be observed predominantly in the loop legs, as discussed above. Since we observe that most of the Fe XVI emission appears to be emitted from loop tops, we conclude that most of the Fe XVI emission observed by the CDS arises from temperatures lower than 2.5×10^6 K.

Mg IX 368.07 Å can be emitted at loop tops in 1×10^6 K loops, or in loop legs for loops with peak temperature of 2×10^6 K or higher. As shown in Sect. 4.1, this dichotomy makes the Mg IX line more difficult to use for the diagnostics of the coronal heating.
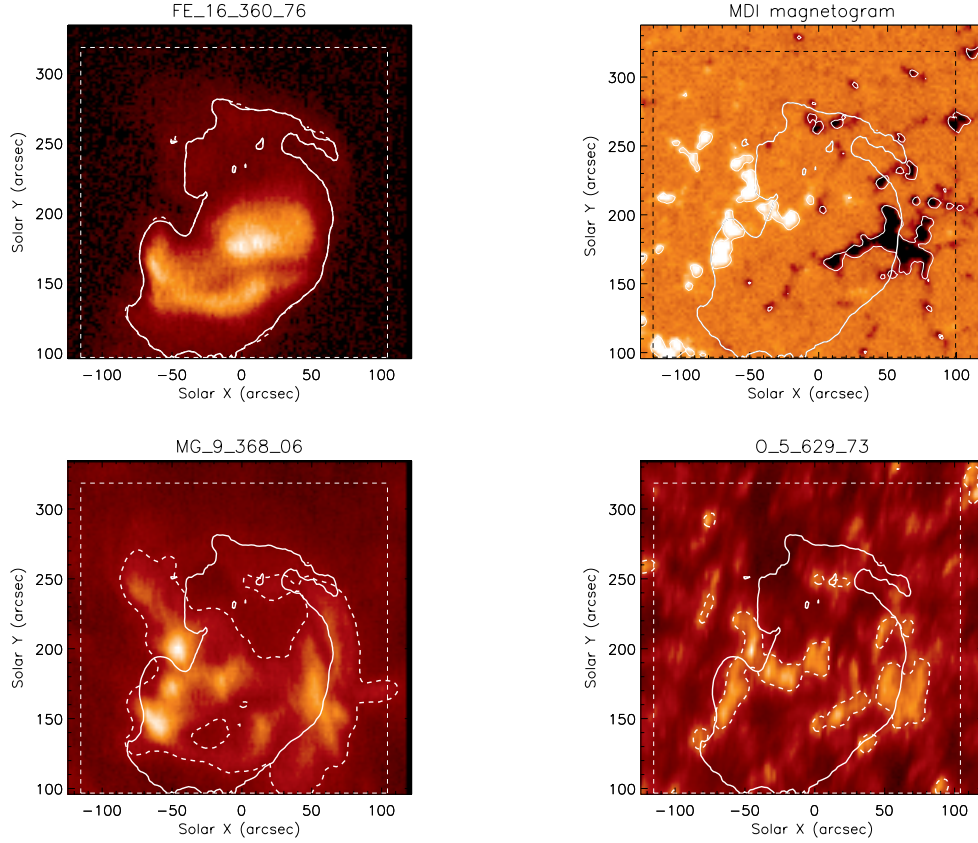
Fig. 1. Comparison of the photospheric magnetic field and projected EUV emission areas in the active region NOAA 8019 on February 28, 1997: **a)** Fe XVI 360.76 Å (*top-left panel*); **b)** MDI magnetogram (*top-right panel*); **c)** Mg IX 368.06 Å (*bottom-left panel*); **d)** O V 629.7 Å (*bottom-right panel*). White thick contour in all panels is the boundary of the Fe XVI emission. White dotted contour in *the two bottom panels* is the boundary of the projected area of the bright Mg IX and O V emission, respectively. White contours in the *top-right panel* are at |90| G level of the magnetic flux density. Straight dashed lines denote the active region box. See Sect. 3 for description.

Table 1. Power indices approximating the integrated Fe XVI line intensity in a single coronal loop as $I_L \propto P^\epsilon$ for different loop apex temperatures.

Temperature interval (K)	ϵ
$1.6 \times 10^6 < T_{top} < 1.9 \times 10^6$	$6 \to 2^*$
$2.0 \times 10^6 < T_{top} < 2.5 \times 10^6$	2
$2.5 \times 10^6 < T_{top} < 3.0 \times 10^6$	$2 \to 1$
$T_{top} > 3.0 \times 10^6$	1

* Variable power index from a to b is denoted $a \to b$.

The third spectral line considered in this paper, O V 629.8 Å, is emitted at transition region temperatures (2.2×10^5 K) and it is assumed that its intensity is always proportional to pressure.

The fourth line, He I 584.3 Å is emitted in the low transition region but its usefulness as a diagnostics is currently limited by difficulty in interpreting helium line intensities, as the helium lines are optically thick and show anomalously high intensities, and a number of possible formation mechanisms have been proposed (Jordan et al. 2005). We will therefore show the results for the He I line but defer its interpretation to a future paper.

The fact that the dependence of the line intensity on pressure is different for lines emitted at transition region temperatures in the loop legs and lines emitted at coronal temperatures at the loop top will be used to explain different values of the power index in the $I_T - \Phi$ relationship in Sect. 5.

3. Data analysis

CDS carries out a daily synoptic observation consisting of nine rasters, $4' \times 4'$ area each, covering the N–S extent along the central meridian. We selected 48 active regions observed in the CDS synoptic data between 1996 and June 1998.

For each active region, we build a mosaic of all rasters that cover the whole region. If the region extends more than $4'$ in the N–S direction or falls on the boundary of two rasters, then all rasters containing the region are included. If the size of the region in the E–W direction is greater than $4'$ or the region falls on the boundary between two synoptic datasets, then that region is observed on two or three consecutive days, and rasters from all the relevant days are included. As a result, we obtain four intensity mosaics in the He I, O V, Mg IX and Fe XVI lines (Fig. 1).

An intensity threshold that defines the boundary between the active region emission and the quiet sun, i.e., that defines the active region area, is selected separately for each spectral line according to the following procedure:

For each spectral line, an intensity distribution of the whole mosaic is plotted, and its mean value I_M and a standard deviation σ is calculated. The active region threshold is defined as the

mean, I_M, plus two standard deviations σ. Averaging the values $I_M + 2\sigma$, we selected a common threshold for all active regions. The following threshold values have been selected for each line, in units of erg cm^{-2} s^{-1} sr^{-1}: 547 for Mg IX, 761 for O V, 1387 for He I, 250 for Fe XVI. This threshold is then applied to all pixels in the mosaic to define the active region area, A, in each of the He I, O V, Mg IX and Fe XVI lines. For the global analysis, a common active region area "box" is defined as a rectangle 30″ wider than the contour of the Fe XVI area. The total intensity is then calculated for each line in each active region for two cases: (a) summing above the active region intensity threshold (i.e., inside the active region contour), and (b) summing over the entire active region box.

The magnetic field information is taken from full disk line-of-sight magnetograms recorded by the MDI instrument on SOHO with a 2″×2″ spatial resolution. We apply the latest MDI calibration available from 15 October 2007 which increases the magnetic flux density by a factor of approximately 1.7 compared to the previous MDI calibration available in 1996–2007. Within the active region box defined earlier, the distribution of the magnetic flux density contains both low values characteristic of the quiet sun, and high values characteristic of active regions. The shape of this distribution, when binned with a 10 G step, is approximately exponential above 90 G, and has a second larger component below 90 G. An example histogram of the magnetic flux density is shown in Fig. 2.

It is important to define correctly the active region magnetic area and active region magnetic flux. Again, we consider two cases. In Case A, we use a fixed threshold of $B_{th} = 90$ G to define the magnetic area of an active region (a threshold of 50 G was used by Schrijver 1987; Fludra & Ireland 2003). As can be seen from Fig. 2, this is approximately where the slope of the histogram changes from the quiet sun component to the active region component. The magnetic area A_Φ of each active region consists of all pixels with the absolute value of the magnetic flux density $|B|$ greater than B_{th}. In Case B, we set $B_{th} = 0$ G and sum all magnetic flux in the entire active region box defined earlier in this section, $\Phi_T = \int |B| dA$.

In both cases, we define a sunspot's magnetic area as containing all pixels with the magnetic flux density $|B|$ greater than 900 G, and exclude the sunspots' magnetic flux from the calculation. The value of 900 G has been obtained empirically from the MDI magnetograms using the new calibration, and was chosen conservatively low to overestimate the sunspot magnetic areas.

4. Results

4.1. Spatial relationship between the EUV emission and photospheric magnetic field

Fludra et al. (1997) pointed out that active region emission at different temperatures seen in the CDS rasters is not co-spatial. In particular, hotter loops at temperatures above 1.6×10^6 K (seen in Si XII 520.7 Å and Fe XVI 360.76 Å emission) are often different from loops seen in spectral lines emitted near 1.0×10^6 K (Mg IX 360.08 Å, Mg X 624.9 Å). Since the CDS synoptic dataset contains both the Mg IX 360.08 Å line (9.5×10^5 K) and the Fe XVI 360.76 Å line (2×10^6 K), the spatial correspondence of emission in different lines can be compared.

Figure 1 shows that the brightest areas in the Fe XVI images are located between the opposite magnetic polarities, and the magnetic field stronger than 90 G is located close to the perimeter of the projected Fe XVI area. This spatial pattern is seen in
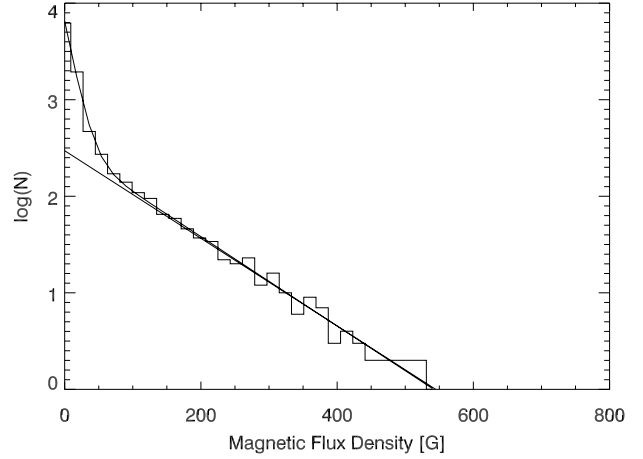
Fig. 2. Histogram of the magnetic flux density in a decaying active region NOAA 08027 (0″, −460″) on 8 May 1997 at 03:16:05 UT. The curved continuous line is a two-component exponential fit in the range 0–500 G. The straight line is the second component.

most of the active regions, implying that the Fe XVI emission comes from tops of coronal loops.

The Mg IX emission (9.5×10^5 K) typically exhibits a more complex spatial distribution: the brightest Mg IX emission is located directly above, or close to, the magnetic field concentrations, while the Mg IX emission between the opposite magnetic polarities is much weaker. This suggests that a significant part of the Mg IX emission comes from the legs of hot coronal loops. However, since it is known from TRACE and SOHO/EIT images in the 171 Å and 195 Å bands that there exist loops with peak temperatures of $1.0-1.2 \times 10^6$ K, a part of the observed Mg IX emission must be coming from the tops of these cooler loops. Thus, the total Mg IX intensity summed over the whole active region contains a mixture of loop-top and loop-leg emission.

As discussed in Sect. 2, line intensity can have a different dependence on pressure depending on the location within the loop: intensity of lines emitted at transition region temperatures is proportional to pressure, P, while the hotter loop-top emission is approximately proportional to P^2. Thus, part of the Mg IX intensity is proportional to P and part is proportional to P^2, making it difficult to use the total intensity summed over an active region as a diagnostic of coronal heating.

For the study of coronal heating, the primary interest centres on the emission coming either entirely from the loop tops or entirely from the transition region in loop legs. Here we assume that the Fe XVI emission represents loop-top emission, while the O V 629.8 Å line represents the transition region in loop legs.

4.2. Line intensity – magnetic flux dependence

Table 2 summarises the range of variability of the total line intensities, I_T, and the total magnetic flux Φ_T in 48 active regions, where both the line intensity and the magnetic flux are taken above the active region threshold of 90 G. Particularly striking is the small variability of the spatially averaged magnetic flux density and average transition region line intensity, compared to the variability of the total magnetic flux and total line intensity.

The total unsigned magnetic flux Φ_T in the range 90–900 G is related to the total magnetic area S_B by a power law $\Phi_T = 6.74 \times S_B^{1.08\pm0.018}$, where the magnetic flux is expressed in Mx and area in cm^2 (Fig. 3a). This is a nearly linear relationship.

Table 2. Range of variability (maximum/minimum ratio) of EUV line intensities and magnetic flux in 48 active regions.

Quantity	He I	O V	Mg IX	Fe XVI	Φ^*
Total	80	80	100	630	120
Average	3	2	2	6.3	1.8

* Φ is summed in the range 90–900 G. "Total" and "Average" refer to area-integrated and area-averaged values, respectively.
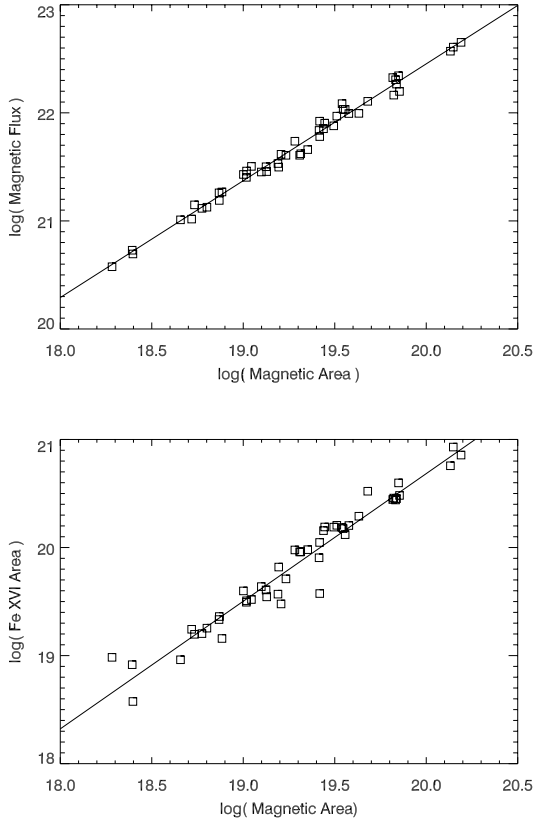
Fig. 3. a) The dependence of the total magnetic flux (Mx) on the magnetic area (cm^2) in 48 active regions (*top panel*); **b)** The dependence of the projected Fe XVI area on the magnetic area (*bottom panel*).

The total magnetic flux in our sample of 48 active regions varies by a factor of 120, and the total area by a factor of 80. However, the averaged magnetic flux density (i.e., total magnetic flux divided by the magnetic area) varies only by a factor of 1.8. This shows that the total magnetic flux increases primarily due to the increase in the magnetic area of the active region, as noted by Schrijver (1987) and Fisher et al. (1998). The increase of the magnetic flux density has only a small contribution to the increase of Φ.

Figure 3b compares the total projected area of the Fe XVI emission, S_{Fe}, with the total magnetic field area, S_B. The projected Fe XVI area is related to the magnetic area by the following power law: $S_{Fe} = 1.16 \times 10^{-3} S_B^{1.18 \pm 0.04}$, where both areas are expressed in cm^2. Again, this is a tight relationship. Global relationships are therefore dominated by the area of the active region.

The relationship between the total line intensity and the total magnetic flux for Case A (above the threshold of 90 G) is shown in Fig. 4. There is a very good dependence of the total EUV line intensity on the total magnetic flux. The fitted power laws are given in Table 3. Power indices are: 0.88 for He I, 0.76 for O V, 0.74 for Mg IX, and 1.32 for Fe XVI. These values are less than 1 for the transition region lines and greater than 1 for the hot coronal line. Best fits are obtained for $I_{HeI} - \Phi_T$ and $I_{FeXVI} - \Phi_T$ relationships, with the Spearman rank correlation coefficient $\rho = 0.96$. Thus, we find that the total magnetic flux Φ_T is a good predictor of both the intensity of the hottest line available in the CDS range (in non-flaring active regions), Fe XVI, and the transition region lines He I and O V. The greatest scatter is seen in the power law for the Mg IX line. Power laws for Case B (the entire active region box) are shown in Fig. 5 and Table 3. The power indices for He I, O V and Mg IX increase slightly by $\approx 1.5\sigma$. The most notable is a significant reduction of scatter for Mg IX. On the other hand, the scatter for Fe XVI increases, confirming our earlier assertion that weak magnetic fields should not be included in the comparison of the magnetic flux with the hot coronal emission (see also Sect. 7.1). Therefore, we do not quote the power index for Fe XVI from Fig. 5d.

5. Interpretation of the power index α

The global relationship $I_T = C\Phi^\alpha$ is only a crude substitute for the $I - B$ relationship for a single loop. Ideally, one should try to resolve individual coronal loops in the EUV or X-ray images, identify their footpoints, align precisely the images with magnetograms and measure the magnetic flux density at the footpoint. While such procedure may occasionally be possible in TRACE images in the 173 Å band, for the majority of data observed with the CDS, EIT and TRACE the coronal EUV emission from adjacent active region loops blends to a degree that makes identification of loops and their footpoints difficult. Therefore, Fludra & Ireland (2003) proposed a method that goes beyond the global $I_T - \Phi$ relationship but does not require the line emission to be spatially resolved. This new method still uses the total EUV intensity integrated over the active region area. However, since the magnetograms already provide a resolved magnetic flux density, typically with $2'' \times 2''$ or smaller pixels, a natural way of progression is to use the information contained in the magnetograms instead of losing it by summing the magnetic flux over the active region area. Following the approach of Fludra & Ireland (2003), we express the total intensity of EUV lines as a sum of all contributions from all coronal loops, leading to the following integral:

$$I_T = \int_\phi \int_L I(\phi, L) h(\phi, L) \, \mathrm{d}L \, \mathrm{d}\phi \qquad (8)$$

where $I(\phi, L)$ is the intensity of individual loops that have the magnetic flux density ϕ at their footpoints and half-length L, and $h(\phi, L)$ is a 2-dimensional histogram of the magnetic flux density and L. The integration limits a, b on ϕ are discussed below. Combining Eqs. (6) and (7), the intensity of a spectral line arising from a single loop has an explicit dependence on the loop length and the magnetic flux density:

$$I(\phi, L) = Q_1 L^\lambda \phi^\delta \qquad (9)$$

where Q_1 is a constant. Therefore, Eq. (8) takes the form:

$$I_T = \int_\phi Q_1 \phi^\delta \left(\int_L L^\lambda h(\phi, L) \, \mathrm{d}L \right) \mathrm{d}\phi. \qquad (10)$$
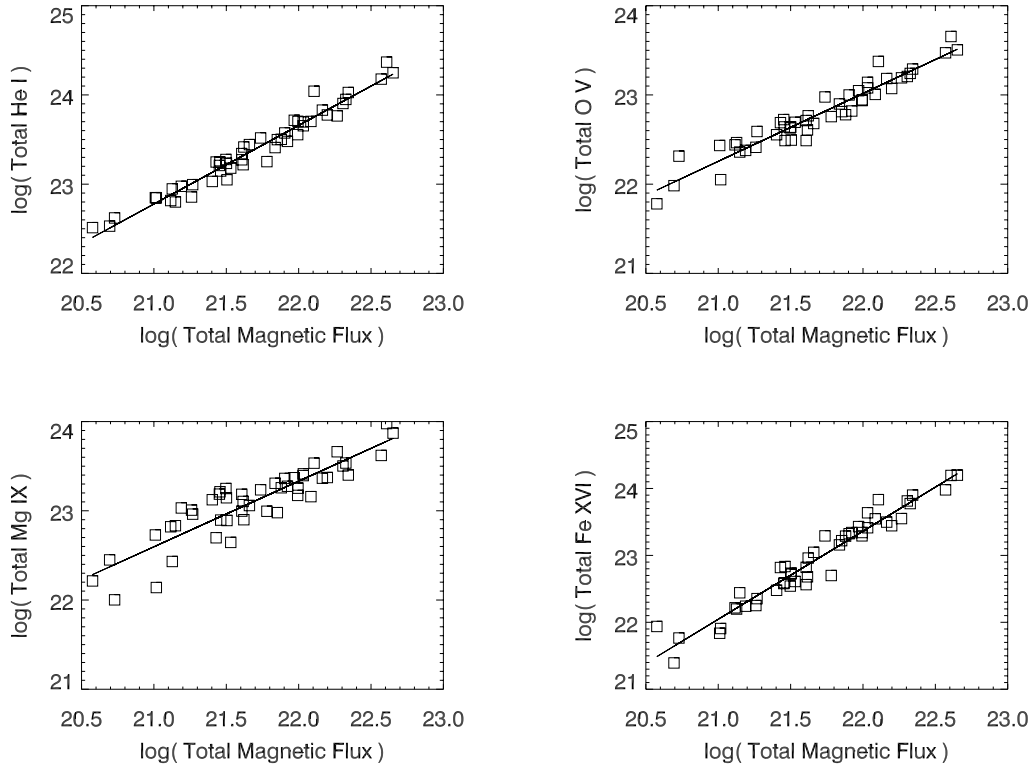
Fig. 4. Total intensity (erg s^{-1} sr^{-1}) of the EUV lines as a function of the total magnetic flux Φ_T [Mx] for 48 active regions. Line intensities are summed above the active region threshold. Only magnetic field in the 90−900 G range is included.

Applying the mean-value theorem to the integral over L in the brackets and denoting $\int h(\phi, L)\, dL = H(\phi)$, we obtain

$$I_T = \int_\phi Q_1 \phi^\delta L_{m,\phi}^\lambda H(\phi)\, d\phi \tag{11}$$

where $L_{m,\phi}$ is a value of the loop length that fulfils the mean value theorem, selected from the range of all values of L present in the active region for a given value of ϕ. As such, $L_{m,\phi}$ can be different for each ϕ and their actual values cannot be known without knowing the exact distribution $h(\phi, L)$. To make Eq. (11) more tractable, we further denote a constant $Q_0 = Q_1 L_m^\lambda$, where L_m is a mean value drawn from all values of $L_{m,\phi}$, such that it gives $\int L_{m,\phi}^\lambda \phi^\delta H(\phi)\, d\phi \approx L_m^\lambda \int \phi^\delta H(\phi)\, d\phi$. This gives the following equation used by Fludra & Ireland (2003) which we will also use in the rest of this paper:

$$I_T = Q_0 \int_a^b \phi^\delta H(\phi)\, d\phi. \tag{12}$$

Fludra & Ireland (2003) also pointed out that the histogram of the magnetic flux density in most active regions can be approximated by an exponential function $H(\phi) = H_0 \exp(-\beta\phi)$ (Fig. 2). Using this property, they demonstrated that the total line intensity integrated over the whole active region area can be expressed through a Laplace transform when the exponential distribution of the magnetic flux density is used in the full range from $a = 0$ to $b = \infty$. The dependence of the total observed intensity on the total magnetic flux can be then expressed in two ways. The first expression is:

$$I_T = Q_0 B_{av}^{\delta-1} \Phi. \tag{13}$$

where δ is the power index for the single loop relationship (Eq. (9)) and $B_{av} = 1/\beta$ is the average magnetic flux density in the interval $(0, \infty)$ when the histogram $H(\phi)$ of the magnetic flux density is an exponential function between 0 and ∞.

The second expression is:

$$I_T = Q_0 H_0^{-0.5(\delta-1)} \Phi^{0.5(\delta+1)} \tag{14}$$

which arises from Eq. (13) because $\Phi = H_0 \beta^{-2} = H_0 B_{av}^2$.

Equation (13) shows that the total intensity is approximately proportional to Φ, but since B_{av} varies from region to region, there cannot be a mathematically justified equality between I_T and Φ, except when $\delta = 1$. Therefore, the global power laws may not be an accurate tool for the study of the coronal heating. However, since several authors used these relationships in the past without any analysis of their suitability, we have carried out a simulation based on real data that attempts to bring an understanding to the interpretation of the power index fitted to these power laws.

We have fitted two exponential components to the actual histograms of the magnetic flux density (Fig. 2) in the 48 active regions and simulated $I_T - \Phi$ power laws for different values of δ above the active region threshold of $B_{th} = 90$ G. The upper limit on the magnetic flux density varies from region to region. The first point to note is that as δ departs from 1.0, a scatter of points becomes apparent in the simulated $I_T - \Phi$ curves, proving that I_T is not a simple function of Φ and that there is no physical basis, other than through the region area, for the two quantities to be precisely related. Nevertheless, a power law index α can be derived for each value of δ (Fig. 6). One would then try to use Fig. 6 to infer the value of δ based on the value of α fitted to the actual observations. This simulation, however, highlights a number of problems. First, the slope of the curve in Fig. 6
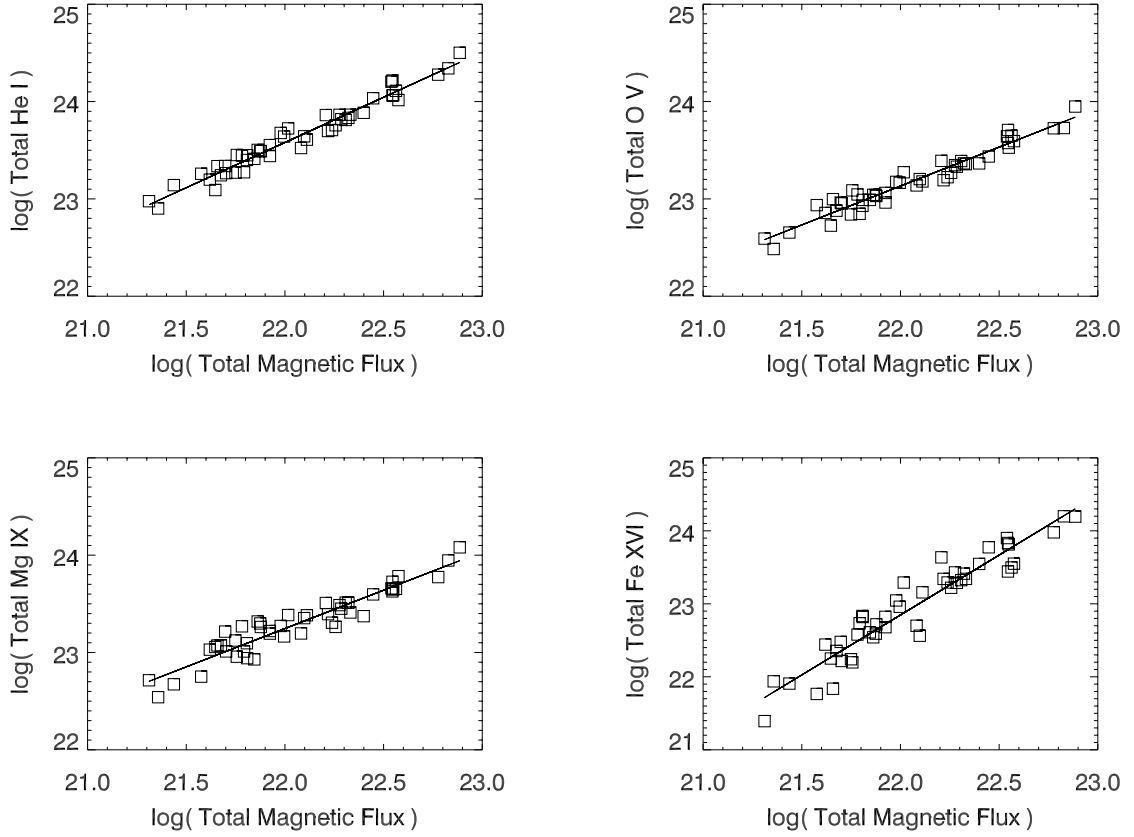
Fig. 5. Total intensity (erg s^{-1} sr^{-1}) of the EUV lines as a function of the total magnetic flux Φ_T [Mx] for 48 active regions. Line intensities and the magnetic flux are calculated in the entire active region box with no lower limit on line intensity and the magnetic flux density. The upper limit on the magnetic flux density is 900 G. Note that the increased scatter for Fe XVI, compared to Fig. 4, demonstrates that weak magnetic fields should not be compared to the Fe XVI emission.

is quite sensitive to the upper integration limit of the magnetic flux density and the curve can become flatter for higher upper limit values. Second, there is a particular problem with values of $\delta < 1$, where α gradually becomes less sensitive to the changes of δ. The lowest value of $\alpha = 0.83$ is still slightly larger than that of 0.76 derived from real data for the O V 629.7 Å line (Table 3). Therefore, it is apparent that this simulation cannot provide a prescription to infer an accurate value of δ from the global power index for the transition region lines (e.g., the O V line). However, as we will show later, a limit $\delta < 1$ for the transition region lines is still useful. For $\delta > 1$, applicable to coronal emission (e.g., Fe XVI line), the relationship between α and δ is a little better determined. For example, $\alpha = 1.3$ measured with accuracy of 4% gives $\delta = 2.3 \pm 0.2$. High accuracy of α is then the key to the estimation of δ, provided that curves such as Fig. 6 are obtained for each analysed data set. We note again that the shape and slope of this curve is sensitive to the integration limits and therefore Fig. 6 does not have a universal application.

However, the forward modelling carried out above can be used to predict approximate values of α if δ is known. In particular, we obtain $\alpha > 1$ for $\delta > 1$, and $\alpha < 1$ for $\delta < 1$. The values of α fitted to the CDS observations are qualitatively consistent with these two cases, as $\alpha_t \approx 0.8$ for transition region lines and $\alpha_c \approx 1.3$ for the Fe XVI coronal line. Because of the proportionality to P^2 and P of coronal and transition region line intensities, respectively, in hydrostatic loop models, we postulate that the
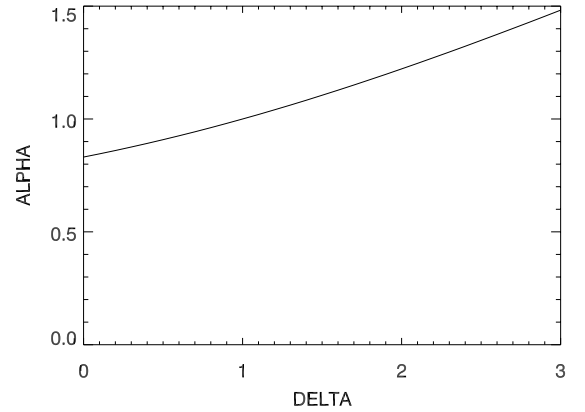
Fig. 6. A simulated dependence of the power index α in the global relationship $I_T \propto \Phi^\alpha$, on the power index δ for individual loops, using exponential fits to real histograms of the MDI magnetic flux density distributions (continuous line). The lower threshold on B is 90 G, the upper limit depends on the actual magnetic field in each region. See Sect. 5 for details.

different values of the power index α arise due to the different dependence of line intensities on pressure.

We emphasise that we consider the method presented in Fludra & Ireland (2003) as a mathematically correct approach to

Table 3. Power law parameters, $I_T = C\Phi^\alpha$, in 48 active regions. Intensities in erg s^{-1} sr^{-1}, Φ in Mx.

Line	He I	O V	Mg IX	Fe XVI
(a) $90 < \phi < 900$				
α	0.88 ± 0.027	0.76 ± 0.033	0.74 ± 0.054	1.32 ± 0.047
C	1.85×10^4	1.92×10^6	1.42×10^7	2.48×10^{-6}
(b) $0 < \phi < 900^{(*)}$				
α	0.93 ± 0.028	0.80 ± 0.029	0.79 ± 0.040	N/A
C	1.37×10^3	3.50×10^5	8.30×10^5	N/A

* In case (b), the magnetic flux Φ and the line intensities are summed in the active region box defined in the text.

determining δ from observations. That method does not rely on the integrated magnetic flux Φ. The consideration of the global power laws has been undertaken in the present paper due to their popular use in the literature, and we have shown that they are not a mathematically sound approach and suffer from the inherent uncertainty in determining the value of δ. Despite these reservations, however, we have been able to derive a rather broad but still useful limit on the volumetric heating rate E_H, as shown in the next section.

6. The heating rate dependence on ϕ

So far we have shown that $\delta_t < 1$ for the transition region lines and $\delta_c > 1$ for the loop-top coronal lines. Using the relationship $\delta_c = 2\delta_t$ that arises from the dependence on P^2 and P for the loop-top and transition region lines (Sect. 2), respectively, we arrive at the following limits on δ_t:

$$0.5 < \delta_t < 1. \tag{15}$$

We note that this relationship depends on the assumption of hydrostatic loops made in Sect. 2 and we address this further in Sect. 7.3.

From Eq. (7) for transition region lines we have: $P \propto I_{tr} \propto \phi^{\delta_t}$, and from Eq. (6) we obtain

$$E_H \propto \phi^{7\delta_t/6}. \tag{16}$$

Thus, denoting $\gamma = 7\delta_t/6$, the heating rate $E_H \propto \phi^\gamma$, where $0.6 < \gamma < 1.1$ and ϕ is the photospheric magnetic flux density at loop footpoints. This result, obtained despite all the shortcomings and limitations of the global power laws, places a useful constraint on the coronal heating mechanism, favouring models that give $E_H \propto B$ (Mandrini et al. 2000). The models that predict $E_H \propto B^2$ are inconsistent with this result.

One would naturally attempt to further narrow down the range for δ and γ to be able to select just one of the heating models reviewed by Mandrini et al. (2000). This can be tried using the simulated $\alpha - \delta$ relationship in Fig. 6 and applying it to the coronal Fe XVI line. Taking the fitted power index $\alpha = 1.3 \pm 0.05$ for Fe XVI (Table 3), we estimate $\delta_c = 2.3 \pm 0.2$. From Sect. 2 we have, therefore, $I_{Fe} \propto P^2 \propto \phi^{2.3}$, which gives $P \propto \phi^{1.15}$, and $E_H \propto \phi^{1.3}$. This value of $\gamma = 1.3$ is a little higher than the upper limit of the range $0.6-1.1$ derived above, but agrees with it almost within 1σ statistical error.

One should note that the temperature dependence of the Fe XVI emissivity is relatively narrow, which makes this line suitable for this analysis in the temperature range $2.0-2.5 \times 10^6$ K. For loop top temperatures lower than 2.0×10^6 K, the Fe XVI intensity dependence on pressure is steeper than P^2 (Sect. 2). If this were the case for many loops in an active region, then the power index γ in the heating rate dependence on ϕ,

$E_H \propto \phi^\gamma$, would be lower than 1.3, entering the range $0.6-1.1$ derived from the transition region lines. Qualitatively then, we can see that it is possible to envisage situations where the result from the Fe XVI would fully agree with the O V result.

A more precise determination is difficult to achieve from the global analysis, as further shown in the next section, where we explore other issues affecting the accuracy of the global power laws. We point out that the above estimates of the power index δ are consistent with the results obtained from forward modelling by Schrijver et al. (2004), and Warren & Winebarger (2006), who derive the heating rate $E_H \propto B$. However, while the forward modelling methods calculate the lengths of all loops and thus provide also the dependence of E_H on L, in this analysis the power index on L cannot be determined, since Eq. (12) depends only on a mean (but unspecified) value of L_m, drawn from all loop lengths in an active region, which is absorbed into the constant of proportionality Q_0.

7. Potential analysis problems

7.1. Interpreting various $I_T - \Phi$ relationships published in the literature

Additional uncertainties in the analysis of the global power laws can arise due to the choice of the analysed area. We have carried out a simulation that illustrates errors introduced to the analysis when the summing or averaging is done over large areas that contain both the quiet sun and active regions. This can arise, for example, when using full disk averages or Carrington maps, as in Benevolenskaya et al. (2002), who divide the Carrington map into strips 1-degree high covering the whole horizontal extent of a Carrington map (360 degrees in longitude), and calculate the total magnetic flux and total EUV intensity in the SOHO-EIT bands summed over the area of each strip. Subsequently, the total values are divided by the size of this area to obtain the averaged intensities and averaged magnetic flux density. The large area of each strip includes a mixture of quiet sun and active regions.

In this simulation we assume that the EUV intensity of individual coronal loops, all with the same length, depends on the magnetic flux density at their footpoint through Eq. (9) and that the EUV emission at active region temperatures is produced for $\phi > B_{th} = 90$ G. We also use an upper limit $\phi < B_{up} = 900$ G to exclude sunspots. We divide the Carrington map into $N = 150$ areas, each containing a mixture of quiet sun magnetic field and active region magnetic field. The quiet sun magnetic flux density distribution is the same in each area, $H_{qs}(\phi) = H_{qs,0} \exp(-\beta_{qs}\phi)$, $\beta_{qs} = 0.1$. The active region distribution is $H_a(\phi) = H_{a,0} \exp(-\beta_a\phi)$, where β_a varies from area to area, from 0.0028 to 0.01, and $H_{a,0}$ is the same in all areas. We begin the simulation by setting the quiet sun component to zero ($H_{qs,0} = 0$), selecting a value for δ, and calculating the total
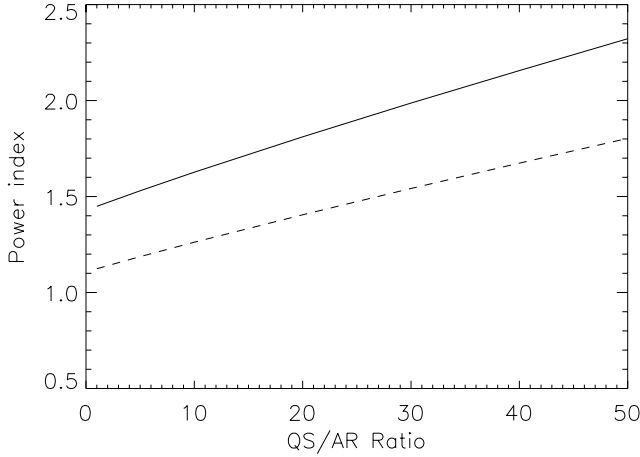
Fig. 7. A simulated dependence of the power index α in the global relationship $I_T \propto \Phi^\alpha$, on the ratio of the quiet sun to active region magnetic flux for $\delta = 2.0$ (continuous line) and $\delta = 1.0$ (dashed line). See Sect. 7.1 for details.

intensity in each area $I_j = \int_{90}^{900} H_{a,0}\phi^\delta \exp(-\beta_j\phi)\mathrm{d}\phi$, and the total flux in each area $\Phi_j = \int_{90}^{900} H_{a,0}\phi \exp(-\beta_j\phi)\mathrm{d}\phi$, $j = 1, ..., N$. The power index α, fitted to the distribution of $I_j - \Phi_j$ is taken as the "real" value of α.

Subsequently, the threshold B_{th} is lowered to 0, and the ratio $R = H_{qs,0}/H_{a,0}$ is varied from 1 to 50, keeping the sum of the quiet sun area and active region area constant. For each value of R the total magnetic flux is calculated in each area, $\Phi_j(R)$ and the power index $\alpha(R)$ is fitted to the distribution $I_j - \Phi_j(R)$, where I_j are the original "real" values of intensities in each area calculated at the beginning of the simulation for $H_{qs,0} = 0$ and $B_{th} = 90$ G. This simulation is equivalent to making an assumption that the entire magnetic flux in the field of view is responsible for the production of the observed EUV intensities.

Figure 7 shows the dependence of the fitted power index values α on the ratio R of the quiet sun to active region magnetic field. For $\delta = 2$, the power index increases from 1.4 to 2.3. For $\delta = 1$, the power index increases from 1.1 to 1.8. High values of R, with the preponderance of the quiet sun magnetic field values, correspond to the condition at the solar minimum and give high values of the power index α. Low values of R simulate the dominance of active regions, representative of the solar maximum, and give low values of the power index α. This simulation therefore demonstrates that the variability of the power index with the solar cycle obtained by Benevolenskaya et al. (2002; their Fig. 6) can be explained by their analysis technique which averages over large areas containing a mixture of quiet sun and active region magnetic fields. Thus, it is not necessary to invoke any change in the coronal heating mechanism with the solar cycle to explain the variability of the power index. The conclusion of this simulation is that when analysing power laws for the spatially integrated hot coronal emission, one should be aware of the effect shown in Fig. 7 and avoid summing or averaging the magnetic field over large areas that include both quiet sun and active region magnetic fields. If possible, the stronger fields of the active region should be separated from the surrounding quiet sun.

A better solution to this problem can be found in van Driel-Gesztelyi et al. (2003) who use a subjective but considerate choice of an active region area. Their procedure places a greater emphasis on the active region flux and thus reduces the

error found in the previous approach. However, some contribution from the quiet sun areas (low magnetic flux density) is still included in their analysis.

In the most stringent approach taken by Schrijver (1987), Fludra & Ireland (2003), and in this paper, a fixed threshold is used to separate the active region magnetic flux from the quiet sun magnetic flux.

7.2. Choosing a threshold for B

Emission is present in a given spectral line when the electron temperature reaches the temperature range in which the line is emitted, around the peak of the line emissivity curves. For illustration purposes, using a static loop scaling laws, the peak temperature T_{top} is proportional to $E_H^{2/7}$, where E_H is the heating rate. If the heating rate is proportional to the magnetic field strength B^γ, as predicted in most coronal heating models, the peak loop temperature is proportional to $B^\epsilon L^\lambda$, where L is the loop length. It is clear from this simple relationship that B has to exceed a certain threshold for T_{top} to reach the threshold above which the line emission is produced, with sufficient intensity to be detected by the spectrometer. For example, CDS observations show no emission in the Fe XVI 360.8 Å line in the quiet sun areas (to within the sensitivity of the instrument). Thus, to a first approximation one can conclude that the quiet sun magnetic field produces a negligible amount of plasma at temperatures above 1.6×10^6 K and therefore the quiet sun magnetic field below approximately 10–20 G should not be taken into account when predicting the emission in the Fe XVI line.

In general, the actual threshold of B above which we can detect the line emission depends on the heating mechanism and instrument sensitivity. We conclude from the above discussion that the global analysis does not provide sufficient information to select the threshold for B, and to provide an unequivocal determination of the heating mechanism.

7.3. Assumptions in loop models

Previous discussion centred on the analysis of the accuracy of the global power laws. Here we mention other possible problems in coronal heating studies arising from the use of hydrostatic loop models in Sect. 2.

Recent papers highlighted puzzling inconsistencies between loop models and observations (e.g., Schrijver et al. 2004; Warren & Winebarger 2006). These studies point out that the emission predicted from quasi-static models does not reproduce the right scaling between observed transition-region and coronal emissions.

It has been shown that the hot coronal emission arises in loops that are in hydrostatic equilibrium (Porter & Klimchuk 1995; Schrijver et al. 2004). If that is true, then the O V emission coming from the footpoints of quasi-static coronal loops with peak temperatures over 1.6×10^6 K will also be quasi-static. If some of cooler loops were in non-equilibrium conditions, then the complexity of the problem would increase, as the observed O V emission would be a sum of static loop emission and dynamic loop emission. Since the fraction of non-equilibrium loops is not known and the analyses published so far do not provide an answer how to diagnose coronal heating mechanism in non-equilibrium conditions, the question whether the differences in global power index values between the O V and Fe XVI emission would then be explainable by the same dependence on pressure as we show for static loops, or a

different explanation would have to be sought, cannot be answered at present. However, we have been able to demonstrate that the measured global power index values are 0.7−0.9 for the transition region lines and ≈1.2−1.3 for the hot coronal emission, and that if one assumes static loop models, this difference can be explained through a dependence of line intensity on pressure.

Constant cross-section of coronal loops has been found in X-ray observations (Klimchuk 2000) and EUV observations (Watko & Klimchuk 2000) and was therefore used in Sect. 2. We point out, however, that simulations by Schrijver et al. (2004) show that models of loops expanding with height provide a better match to measured X-ray fluxes. This highlights yet another problem in comparing loop models with observations to which loop modellers do not have an answer at present. However, should the loop cross-section increase with height in contradiction to direct observations, the modelled temperature distributions along the loop in the low transition region ($T_e = 2 \times 10^5$ K) are relatively insensitive to a variable cross-section (Figs. 4 and 5 in Vesecky et al. 1979). Therefore, we use Eq. (4) that assumes a constant cross-section.

The data available to us are not suitable for an independent testing of these assumptions – we simply show these assumptions allow us to explain the measured global power index values. Given a number of other simplifications present in the global power law analysis, small deviations from the assumptions of static loops or varying loop cross-section would still be consistent with the different values of the power index.

To summarise, observations in different transition region lines show that the global power index is always less than 1.0, while the power index for the hot coronal emission is greater than 1.0. We show that static loop models allow us to explain this difference by a different dependence of line intensities on pressure, where transition region line intensities are proportional to P, while the coronal Fe XVI line intensity is proportional to P^2.

8. Discussion and summary

The total magnetic flux Φ_T is found to be a good predictor of the intensity of some EUV lines observed in active regions by the SOHO-CDS spectrometer. In particular, the total intensities of the three EUV lines of interest for this paper, and with the least amount of scatter, are related to the total magnetic flux by the following power laws (see Fig. 4): $I_{HeI} = 1.85 \times 10^4 \Phi^{0.88}$, $I_{OV} = 1.92 \times 10^6 \Phi^{0.76}$, and $I_{Fe} = 2.48 \times 10^{-6} \Phi^{1.32}$.

Thus, Φ provides an independent check on observed line intensities, allowing, for example, to explore changes of elemental abundances by comparing I_T and Φ. This is attractive in view of the long-standing problem of the scaling of coronal abundances and their dependence on the First Ionization Potential (e.g., Fludra & Schmelz 1999; Fludra et al. 1999). Such power laws can also be used to cross-calibrate different instruments observing similar spectral lines, for example, the SOHO CDS and Hinode EIS.

Conversely, these power laws can also be used to estimate the total magnetic flux from the EUV intensities. The EUV emission as a proxy for the magnetic field can be used for active regions approaching the limb, when the magnetic field cannot be measured reliably. Hot coronal lines, e.g., Fe XVI, are more useful than the transition region lines on the limb in this case, as the coronal emission extends to heights of tens of thousands km.

While measurements of global power laws for the coronal X-ray emission have been done by many authors (see Sect. 1)

and consistently have values 1.1−1.3, i.e., greater than 1.0, such power laws for transition region lines are relatively rare. Power index values for all our three transition region lines are 0.7−0.9, i.e., less than 1.0, and they agree with a value of $\alpha = 0.69$ obtained for a C II line in solar active regions by Schrijver (1987). They also obtained $\alpha = 0.97$ for a Mg X line which has only slightly higher formation temperature than the Mg IX line discussed in this paper and thus, like the Mg IX line, represents a mixture of loop-top and loop-leg emission. Additionally, measurements of transition region C III, O IV, and O VI intensities in solar active regions were made by Schrijver et al. (1985), but that paper explored only intensity-intensity relationships without comparing them to the magnetic field. However, when we combine their $I − I$ power laws for C III and O IV as a function of C II with the above-mentioned dependence of C II on Φ from Schrijver (1987), this gives $I_T − \Phi$ power index values for C III and O IV that are also significantly less than 1.0.

One of the important applications of these global power laws would be their potential use to distinguish between coronal heating models. In this paper we pointed out problems in the analysis of the coronal heating from a global $I_T − \Phi$ power law. Using a method presented in Fludra and Ireland (2003) and simulations based on real data we have shown that it is not mathematically justified to expect an equality $I_T = C\Phi^\alpha$. Further uncertainties arise from limits in the integration of the magnetic flux density and the assumptions one makes on the spatial distribution of the magnetic field, which means it is difficult to get back to the exact heating rate dependence of B. These findings are very important for the coronal heating debate, as many past analyses did not consider these issues in detail.

We discussed thoroughly the interpretation of the global power index α for the coronal emission, using the Fe XVI line. We demonstrate that one needs to carry out detailed, precise simulations using the distribution of magnetic flux densities to be able to use the global power index α to deduce the value of the power index δ for individual coronal loops. None of the previously published analyses of global power laws $I_T − \Phi$ have done such calculation and this is the first time that such analysis has been carried out. It shows that the diagnostic accuracy of the global power laws may be limited, especially for transition region lines. Deeper insights into the coronal heating mechanism can be obtained from forward modelling as done, e.g., by Schrijver et al. (2004) and Warren & Winebarger (2006).

Despite the approximate nature and uncertainties inherent in the analysis of the global power laws, some constraints can be placed on the coronal heating models. The fact that the power index $\alpha < 1$ for the transition region lines and $\alpha > 1$ for the coronal lines originating at loop tops, combined with the assumption of hydrostatic loops, places a limit $0.5 < \delta_t < 1$ on the power index in Eq. (9) for transition region line intensities from individual loops, $I_{tr} \propto \phi^{\delta_t}$. This, from the scaling laws, gives the heating rate $E_H \propto \phi^\gamma$, where $0.6 < \gamma < 1.1$. The dependence on L has not been determined in this analysis. While the derived range for γ is quite large, it allows one to distinguish between models that predict $E_H \propto B$ and $E_H \propto B^2$ dependence of the heating rate. The upper limit of this range is in agreement, within statistical error, with an estimate $E_H \propto \phi^{1.3}$ obtained solely from the power law for the coronal Fe XVI emission. Clearly, the $E_H \propto B^2$ models are inconsistent with these results. This conclusion agrees with results of forward modelling studies done by Schrijver et al. (2004), and Warren & Winebarger (2006).

An interesting example of issues arising in the global power law analysis is given in Pevtsov et al. (2003, their Fig. 1) who present such a power law for X-ray radiance spanning 12 orders

of magnitude from solar targets to stellar objects. This relationship illustrates a huge range of magnetic flux and X-ray emission values in the universe and shows that the two quantities are intimately connected. From the discussion of global relationship presented above it appears that 12 orders of magnitude change in the total magnetic flux and X-ray emission is mostly caused by the geometry, i.e., the change of the magnetic area and the volume of the emitting plasma. The bulk of this dependence is due to the size of the emitting regions, i.e., the magnetic field acts as a container for the emitting plasma.

That 12-orders of magnitude relationship is a collection of data points from different categories of objects and instruments, based on different data processing methods. Pevtsov et al. (2003) point out two groups of objects comprising the $I_X - \Phi$ distribution in their Fig. 1 that are subject to significant uncertainties: the full solar disk averages, when considered on their own, have a power index of 2.1 which is unusually high and could be explained by the same reasoning we applied in Sect. 7.1, i.e., the inclusion of low-value magnetic flux areas that do not contribute to the X-ray emission. On the other hand, the group of solar bright points have the power index of 0.9, which is unusually low for X-ray emission. Fitting all data groups gives an average power index of 1.13 that averages all random and systematic uncertainties. For reasons discussed earlier, the confidence in fitting this complex dataset would be greater if each of the separate categories of points comprising that figure agreed with the average fit.

Another example of global power laws comes from a paper by Warren & Winebarger (2006) who carry out a very detailed forward modelling and deduce the heating rate dependence on B through computing magnetic field extrapolations and hydrostatic loop models. As part of this investigation, they also derive a power index of 1.57 between the X-ray signal in Yohkoh SXT filter measurements and the total magnetic flux in solar active regions. This value is significantly larger than the power index of 1.19 derived by Fisher et al. (1998) also from Yohkoh SXT observations of active regions. Such differences would be highly significant if they referred to identical quantities, however, in this case the difference can most likely be attributed to different quantities used in both papers. Fisher et al. (1998) converted a thin aluminum (Al.1) filter signal to $1-300$ Å X-ray luminosity. On the other hand, Warren & Winebarger (2006) used the signal in both thin aluminum and a sandwich AlMg filters as measured by the instrument ("Data Number" per second). Thus, the resulting global power index values in the two papers should not be compared directly. Since the global power index in Warren & Winebarger (2006) is a useful but secondary quantity, the differences discussed above serve only as an illustration that global power laws can have different power index depending on whether one uses a direct instrument signal or converts it to a physical quantity such as luminosity.

In summary, from the analysis of 48 solar active regions observed by the Coronal Diagnostic Spectrometer on SOHO and the MDI magnetograms we have found:

1. The total photospheric magnetic flux in the $90-900$ G range is nearly proportional to the magnetic area.
2. The observed spatial distributions of the Fe XVI brightness suggests that most of the emission in the Fe XVI line originates at loop tops and that the temperature at loop apex is below 2.5×10^6 K.
3. A significant part of the 1.0×10^6 K emission in the Mg IX line originates in loop legs. Mg IX emission integrated over the active region area is a mixture of a loop-top and loop-leg emission.

4. A power law dependence between four total EUV line intensities and the total magnetic field flux was derived. In particular, the power index for the Fe XVI intensity dependence on Φ is similar to the power index previously found for X-ray emission. The best $I_T - \Phi$ correlation exists for transition region lines He I 584.3 Å, O V 629.7 Å, and hot coronal lines (Fe XVI 360.8 Å, $T_e \approx 2 \times 10^6$ K). The total photospheric magnetic flux is a good predictor of these EUV line intensities in most active regions.
5. These relationships derived from SOHO-CDS data can be applied to verify the intensity calibration of other space instruments, e.g., Hinode-EIS spectrometer, through the measurement of the magnetic flux in a number of active regions.
6. Another application of the $I_T - \Phi$ relationship is the ability to estimate the total magnetic flux when the magnetic field observations are missing, or for active regions near the limb, where the magnetic field cannot be reliably measured while the coronal EUV/X-ray emission extends above the limb and the total intensity over the entire region can be derived.
7. We have discussed the diagnostic capability of the power index, α, in the global relationship, $I_T - \Phi$. We have shown that in solar active regions the inverse problem of deriving the $I - B$ relationship for single loops from the global $I_T - \Phi$ relationship is mathematically ill-conditioned for the transition region lines, where $\delta < 1$. The difficulty arises due to the exponential nature of the magnetic flux density distribution, combined with the expected $I(\phi) \propto \phi^\delta$ dependence. The same problem for the coronal lines is a little better determined, but would require a very high accuracy (5%) of measuring the power index α, and an accurate simulation of the $\alpha - \delta$ relationship specific to each dataset, to provide a diagnostics of the coronal heating mechanism.
8. We have demonstrated that the global analysis of hot, coronal emission may lead to incorrect and variable values of the power index α if the analysed area is too large, containing a significant part of the quiet sun in addition to the active region emission.
9. We have shown from forward modelling that the difference in power index values for the transition region lines ($\alpha < 1$) and hot coronal lines ($\alpha > 1$) is qualitatively in agreement with hydrostatic loop models, reflecting a different dependence of line intensities on pressure.
10. Despite the shortcomings and uncertainties inherent in the global analysis, we have shown under the assumption of hydrostatic equilibrium that the volumetric heating rate $E_H \propto \phi^\gamma$, where $0.6 < \gamma < 1.1$. A separate estimate from the Fe XVI line gives $\gamma \leq 1.3$.

References

Benevolenskaya, E. E., Kosovichev, A. G., Lemen, J. R., Scherrer, P. H., & Slater, G. L. 2002, ApJ, 571, L181

Demoulin, P., van Driel-Gesztelyi, L., Mandrini, C. H., Klimchuk, J. A., & Harra, L. 2003, ApJ, 586, 592

Dere, K. P., Landi, E., Mason, H. E., et al. 1997, A&AS, 125, 149

Fisher, G. H., Longcope, D. W., Metcalf, T. R., & Pevtsov, A. A. 1998, ApJ, 508, 885

Fludra, A., & Ireland, J. 2003, A&A, 398, 297

Fludra, A., & Schmelz, J. T. 1999, A&A, 348, 286

Fludra, A., Brekke, P., Harrison, R. A., et al. 1997, Sol. Phys., 175, 487

Fludra, A., Saba, J. L. R., Henoux, J.-C., et al. 1999, Coronal Abundances, in The Many Faces of the Sun, ed. K. T. Strong, et al. (Springer), 89

Fludra, A., Ireland, J., Del Zanna, G., & Thompson, W. T. 2002, Adv. Space Res., 29, 361

Golub, L., Maxson, C., Rosner, R., Vaiana, G. S., & Serio, S. 1980, ApJ, 238, 343

Gurman, J. B., Withbroe, G. L., & Harvey, J. W. 1974, Solar Phys., 34, 105

Hammer, R. 1992, in: Seventh Cambridge Workshop on Cool Stars, Stellar Systems and the Sun, ed. M. S. Giampapa, & J. A. Bookbinder, ASP Conf. Ser., 26, 528

Jordan, C., Smith, G. R., & Houdebine, E. R. 2005, MNRAS, 362, 411

Klimchuk, J. A. 2000, Sol. Phys. 193, 53

Mandrini, C. H., Demoulin, P., & Klimchuk, J. A. 2000, ApJ, 530, 999

Martens, P. C. H., Kankelborg, C. C., & Berger, T. E. 2000, ApJ, 537, 471

Pevtsov, A. A., Fisher, G. H., Acton, L. W., et al. 2003, ApJ, 598, 1387

Porter, L. J., & Klimchuk, J. A. 1995, ApJ, 454, 499

Rosner, R., Tucker, W. H., & Vaiana, G. S. 1978, ApJ, 220, 643

Saar, S. H. 2001, Proceedings of the 11th Cool Stars, Stellar Systems and the Sun, ASP Conf. Ser., 223, 292

Schrijver, C. J. 1987, A&A, 180, 241

Schrijver, C. J., & Aschwanden, M. J. 2002a, ApJ, 566, 1147

Schrijver, C. J., & Aschwanden, M. J. 2002b, ApJS, 142, 269

Schrijver, C. J., Zwaan, C., Maxson, C. W., & Noyes, R. W. 1985, A&A, 149, 123

Schrijver, C. J., Sandman, A. W., Aschwanden, M. J., & DeRosa, M. L. 2004, ApJ, 615, 512

Summers, H. P. 1993, JET Joint Undertaking Report, JET-IR(93)06

van Driel-Gesztelyi, L., Demoulin, P., Mandrini, C. H., Harra, L., & Klimchuk, J. A. 2003, ApJ, 586, 579

Vesecky, J. F., Antiochos, S. K., & Underwood, J. H. 1979, ApJ, 233, 987

Warren, H. P., & Winebarger, A. R. 2006, ApJ, 645, 711

Watko, J., & Klimchuk, J. A. 2000, Sol. Phys., 193, 77

Yashiro, S., & Shibata, K. 2001, ApJ, 550, L113